Click Here for Full Article

Exploring sources of magnetospheric plasma using multispecies MHD

D. T. Welling[1] and A. J. Ridley[2]

[1] A persistent, unresolved problem in terrestrial magnetospheric physics is determining the dominant source and associated entry mechanism for plasma in the Earth's magnetosphere. This study uses the multispecies MHD code, Block Adaptive Tree Solar Wind Roe-Type Upwind Scheme (BATS-R-US), to investigate this issue. Two proton species, ionospheric origin and solar wind origin, are defined in the system and the evolution of each population is followed under different idealized solar wind conditions. It is found that during southward oriented interplanetary magnetic field (IMF), the dominant source is ionospheric plasma entering deep down tail through reconnecting field lines. During northward IMF, the dominant source is solar wind plasma entering through the flanks of the magnetosphere. This two-mode behavior is tested through data-model comparisons of real world simulations. Comparisons of model results against Los Alamos National Laboratory Magnetospheric Plasma Analyzer density, pressure, and inferred oxygen content support the conclusions of the idealized results.

Citation: Welling, D. T., and A. J. Ridley (2010), Exploring sources of magnetospheric plasma using multispecies MHD, *J. Geophys. Res.*, *115*, A04201, doi:10.1029/2009JA014596.

1. Introduction

[2] The dominant source and entry mechanism for plasma sheet and ring current particles is a topic that has been the focus of many studies over the past several decades. A simplified summary of the debate yields two possible sources, solar wind entry versus ionospheric outflow into the plasma sheet. Two entry paths are considered to deliver mass from these sources to the inner magnetosphere, either vertical transport with convecting magnetic field lines into the plasma sheet then into the ring current region or flank entry into the plasma sheet through a variety of mechanisms. Unraveling this mystery is of utmost importance to achieve a thorough understanding of the terrestrial magnetosphere.

[3] Early evidence for ionospheric sources came in the form of O^+ measurements in these regions as presented by *Shelley et al.* [1974]. Confirming the first measurements were studies that found O^+ composition increasing during increased solar and magnetospheric activity [e.g., *Lennartsson and Shelley*, 1986; *Nosé et al.*, 2003; *Denton et al.*, 2005]. Others have taken a step further and concluded that ionospheric outflow is indeed the dominant source for sheet and ring current plasma [*Chappell et al.*, 1987]. Many of these studies assert that outflowing ionospheric plasma enters the sheet from above and below as they convect with magnetic field lines [e.g., *Chappell et al.*, 2000].

[4] Solar wind sources remain a probable alternative, however. Measurements of the boundary layers and plasma sheet [*Eastman et al.*, 1985], especially detections of He^{++} [*Lennartsson*, 2001], imply plasma from solar wind origins. The entry mechanism is not yet agreed upon, with some presenting data and model work supporting entry through the dayside reconnection region [*Lennartsson*, 2001; *Winglee*, 2003; *Moore et al.*, 2005], and others supporting flank entry [*Eastman et al.*, 1985; *Peroomian and El-Alaoui*, 2008].

[5] This work utilizes the magnetohydrodynamic (MHD) approach to numerical modeling of the magnetosphere to investigate this problem. Simulations of idealized solar wind and magnetospheric conditions are first used to assess the importance of ionospheric and solar wind plasma sources. These results are then tested with simulations of real world events. Data-model comparisons are performed to evaluate the veracity of the conclusions drawn from the models.

2. Methodology

[6] In order to gain a simple, first-order understanding of the plasma entry process into the magnetosphere, idealized simulations are carried out utilizing the Block Adaptive Tree Solar Wind Roe-Type Upwind Scheme (BATS-R-US) MHD code [*Powell et al.*, 1999; *De Zeeuw et al.*, 2000]

[1]Los Alamos National Laboratory, Los Alamos, New Mexico, USA.
[2]Department of Atmospheric, Oceanic and Space Sciences, University of Michigan, Ann Arbor, Michigan, USA.

coupled to a serial ionosphere electrodynamics solver [*Ridley and Liemohn*, 2002; *Ridley et al.*, 2004] through the Space Weather Modeling Framework (SWMF) [*Tóth et al.*, 2005, 2007]. To simplify these simulations, constant solar wind and interplanetary magnetic field (IMF) are used. Additionally, the dipole axis is aligned with the terrestrial spin axis, removing the effects of the dipole's tilt toward or away from the Sun. The results are analyzed by examining the magnetospheric configuration, plasma flow paths, and the destination of plasma originating from the solar wind and ionosphere.

[7] The BATS-R-US model is highly configurable, and the settings used for this study are described here. The inner boundary of the modeling domain is set at 2.5 R_E. This radius is chosen to encompass as much as the inner magnetosphere as possible but prevent the Alfven wave speed, which is proportional to the magnetic field strength, from reaching values that require diminutive time steps. A consequence of the inner boundary location is that all terrestrial magnetic field lines map to ±50° latitude or higher. Hence all field lines of interest are mapping to the near polar ionosphere. There is no imposed minimum density or pressure in the code, so if a negative value is reached, the code stops with an error.

[8] Numerical diffusion is a concern in all numerical models; if there is too much, it becomes dominant over the physical processes, resulting in incorrect simulation results. Several steps are taken here to ensure that the diffusion is under control. The Rusanov solver [*Rusanov*, 1961] is used with a mixing of the minmod (robust, but diffusive) and monotonized central (MC, nondiffusive, but less stable) flux limiters. Blending the two limiters limits diffusion but retains model robustness. Numerical diffusion is proportional to grid cell size, so a high resolution ($\frac{1}{8}R_E$, approximately 1.9 million cells, described in detail below) is used in this study, particularly in regions of interest. This ranks on the higher end of the spectrum compared to other contemporary studies using BATS-R-US (for comparison, *Zhang et al.* [2007] uses a minimum resolution of $\frac{1}{4}R_E$ with 300,000 grid cells, *Tóth et al.* [2007] uses $\frac{1}{4}R_E$ with one million grid cells, and *Ridley et al.* [2002] uses $\frac{1}{8}R_E$ and 800,000). Finally, the "Boris Correction" factor [*Boris*, 1970; *Gombosi et al.*, 2002] is employed to artificially reduce the speed of light by a factor of 50. In semirelativistic MHD, this slows the maximum wave speed, thus increasing the minimum timestep. Because numerical diffusion is dependent on the maximum wave speed in the simulation [*Powell et al.*, 1999; *Lyon et al.*, 2004], the Boris factor inhibits diffusion as well. All of these methods combined work to reduce the diffusion in the simulations presented here.

[9] Single fluid, ideal magnetohydrodynamics is incapable of distinguishing between plasma of different sources. Because of this, it is necessary to switch from single fluid BATS-R-US to the multispecies version, described by *Ma et al.* [2002]. As opposed to treating the entire plasma population as a single fluid, the number density is divided into several different species, as defined by the model user. This creates a new set of MHD equations that are solved by the model (equation (1)). With a separate continuity equation for each species, the different populations may now be traced through the simulation domain. However, there remains only a single momentum and energy equation, so the solution is still, essentially, single-fluid.

$$
\begin{pmatrix}
\dfrac{\partial \rho_1}{\partial t} + \nabla \cdot (\rho_1 \mathbf{u}) = 0 \\
\vdots \\
\dfrac{\partial \rho_n}{\partial t} + \nabla \cdot (\rho_n \mathbf{u}) = 0 \\
\rho_{total} = \rho_1 + \rho_2 + \cdots + \rho_n \\
\dfrac{\partial \rho_{total} \mathbf{u}}{\partial t} + \nabla \cdot (\rho_{total} \mathbf{uu} - \mathbf{BB}) + \nabla p_{total} = 0 \\
\dfrac{\partial e}{\partial t} + \nabla \cdot (\mathbf{u}e + \mathbf{u}p_{total} - \mathbf{BB} \cdot \mathbf{u}) = 0 \\
\dfrac{\partial \mathbf{B}}{\partial t} + \nabla \cdot (\mathbf{uB} - \mathbf{Bu}) = 0
\end{pmatrix}
\quad (1)
$$

[10] For the purposes of investigating magnetospheric plasma sources, two proton species are defined in the study, solar wind and ionospheric protons. At the upstream boundary, the plasma is set to be nearly 100% solar wind protons; at the inner boundary it is 100% ionospheric protons. Each simulation is initialized with pure ionospheric plasma. This setup furnishes an easy assessment of if and how solar wind plasma enters the magnetosphere.

[11] Figure 1 shows the grid layout used in the MHD simulations. Near-body resolution is $1/8R_E$; geosynchronous satellites reside in the region of $1/4R_E$ resolution. Higher-resolution regions are expanded tailward to better capture tail dynamics. This setup yields approximately 1.9 million grid points.

3. Idealized Results

3.1. Southward IMF

[12] The first simulation was performed with a constant southward IMF configuration. The solar wind velocity and density were held constant at average values (450 km s^{-1} and 8.7 cm^{-3}). As with all simulations in this study, 5000 iterations in local time stepping mode [*Ridley et al.*, 2002] are used to accelerate the system toward a steady state. In this mode, each cell within the computational domain is allowed to use its own timestep depending on the dynamics in the cell. After this phase, the simulation was allowed to run in time-accurate mode (uniform timestep throughout the domain) until any lingering, large-scale dynamics settled. In this mode, steady state was achieved well before the 8 h time limit.

[13] Figure 2 (left) shows the configuration and content of the magnetosphere during southward ($B_z = 10$ nT) IMF conditions in the Y = 0, or noon-midnight meridional, plane. The inner boundary is denoted by the black circle of radius 2.5 R_E, and the black lines show the field topology (line density does not necessarily imply field strength). Contours show the percent of plasma that is of solar wind origins (solar wind species from the upstream boundary.)

[14] Figure 2 demonstrates that when viewing from the Y = 0 plane, there is no solar wind entry into the central plasma sheet or inner magnetosphere in the BATS-R-US model during southward oriented IMF. Plasma of ionospheric origin appears to dominate the inner and outer magnetosphere through the plasma sheet well past the tail reconnection point. The solar wind plasma begins to mix
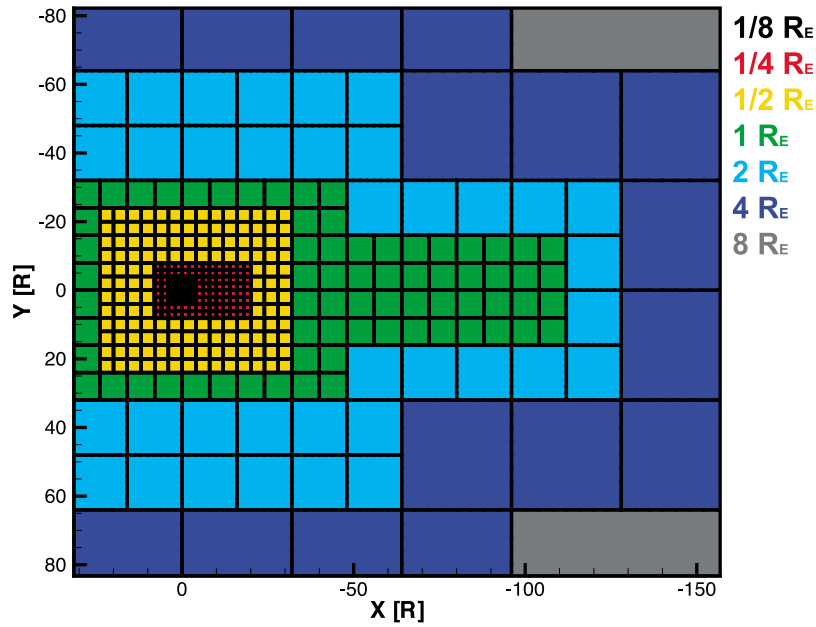
Figure 1. Grid used for the Block Adaptive Tree Solar Wind Roe-Type Upwind Scheme (BATS-R-US) code as seen in the Z = 0 plane. The grid extends to ±128 R_E in the Y and Z directions and from 32 R_E to −224 R_E in the X direction. The grid is symmetric such that a slice in the Y = 0 plane would look identical to this slice. Resolution is denoted by color and corresponds to the key to the right of the grid.

along the magnetopause but does not penetrate deeply into the magnetosphere.

[15] Figure 3 illustrates how the ionosphere species enters the plasma sheet and ring current regions. This Y = 0 slice shows pressure as black contour lines and a single streamline of inner boundary-originating plasma. Color of the

streamline shows the temperature of the plasma along its path.

[16] Ionosphere plasma is first sucked away from the inner boundary by pressure gradient forces. It immediately begins to **E** × **B** drift with the convecting magnetic field lines toward the nightside. Low pressure in the lobes pulls the ionospheric plasma down tail, where it convects toward the
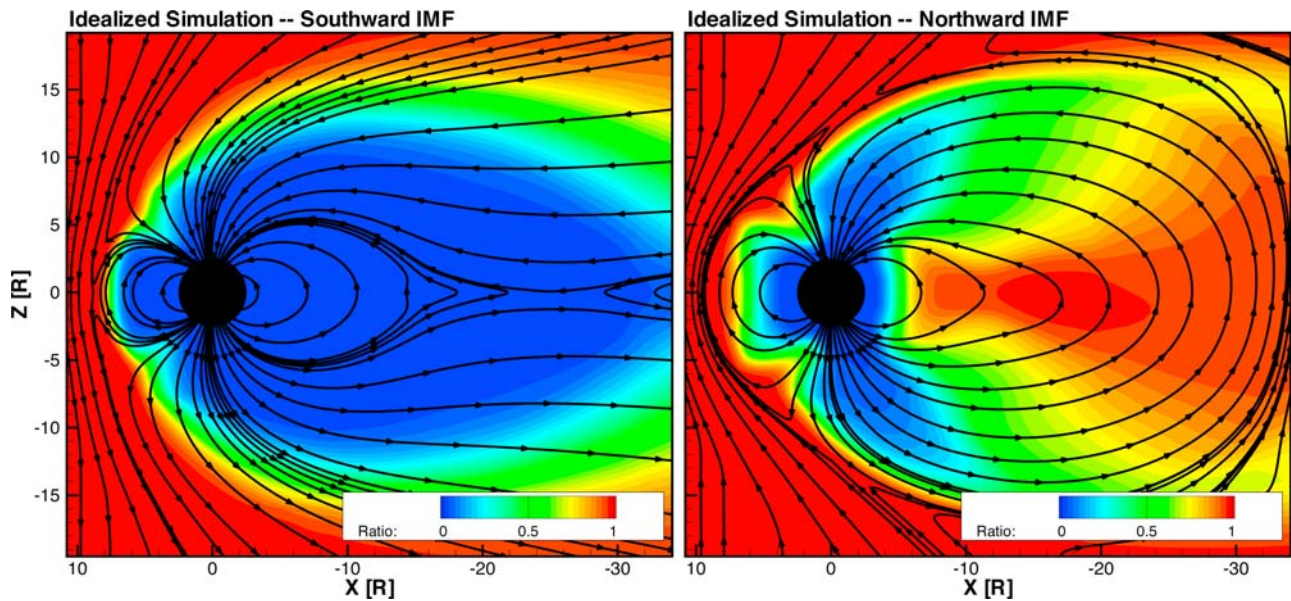

Figure 2. Slices of the magnetosphere in the Y = 0 (noon-midnight meridional) plane (left) during southward interplanetary magnetic field (IMF) B_z conditions and (right) during northward IMF B_z. The dark circle is the inner boundary of the simulation domain (a sphere of $2.5R_E$); black lines show magnetic field configuration. Contours show percent of the plasma that is the solar wind species.
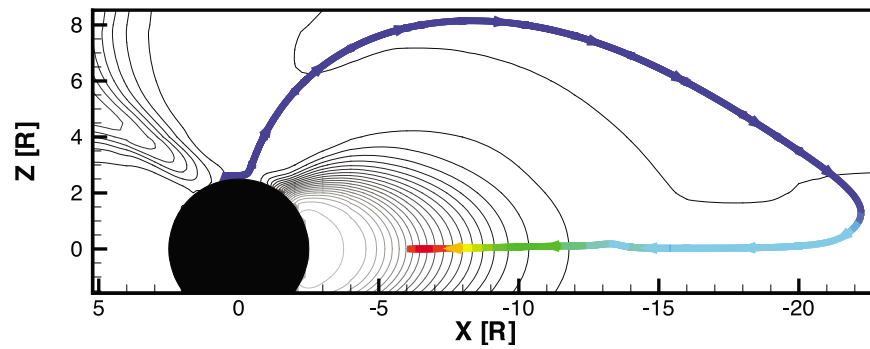
Figure 3. A slice of the magnetosphere in the Y = 0 plane with a single plasma streamline from the ionosphere to the plasma sheet. The dark contours are equipressure lines. Color along the streamline shows the temperature, in electron volts, of the plasma as it is transported into the tail.
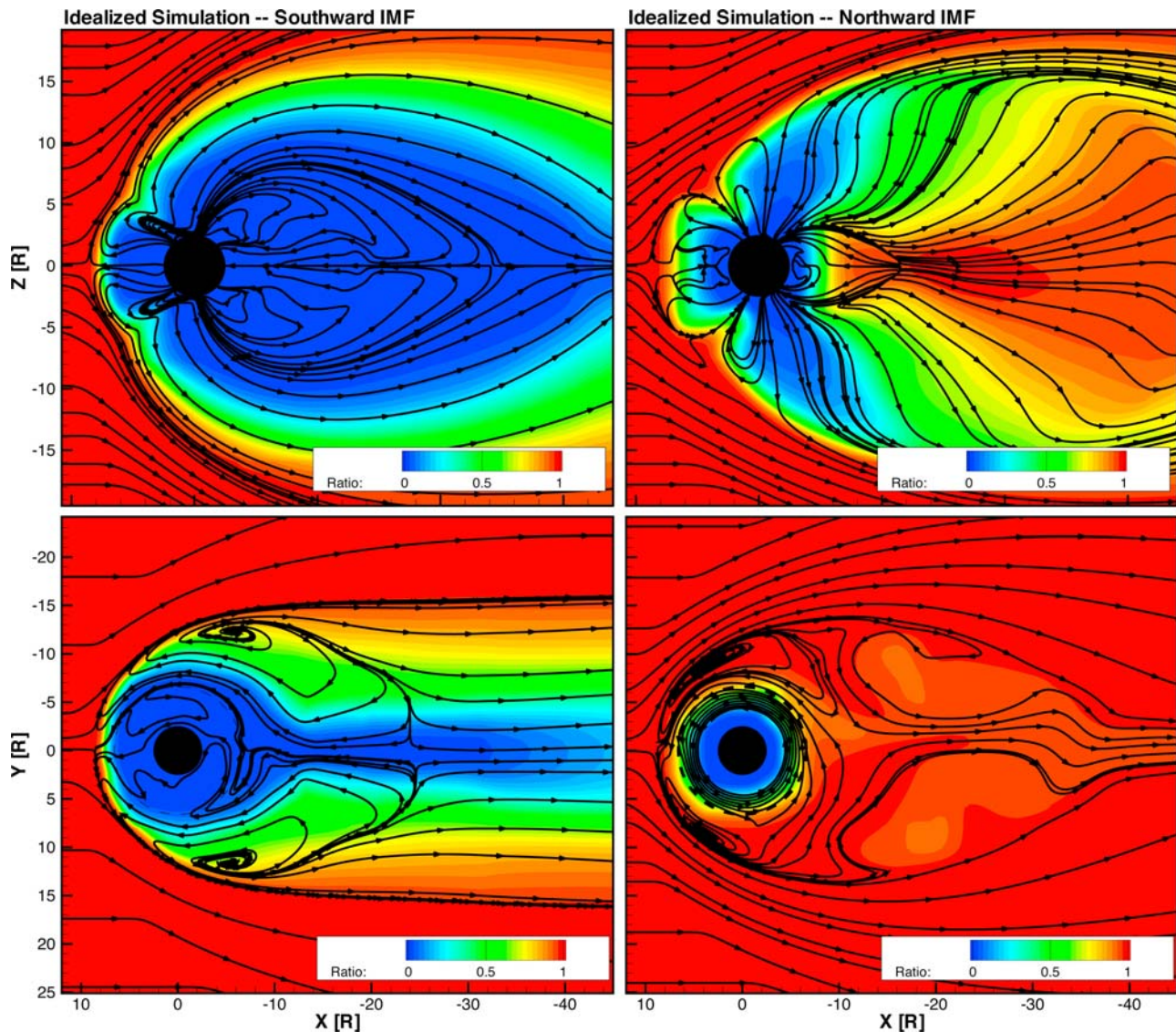

Figure 4. Slices of the magnetosphere in the (top) Y = 0 and (bottom) Z = 0 (equatorial) planes (left) during southward IMF B_z conditions and (right) during northward IMF B_z. Contours show percent of plasma that is solar wind species. Black lines show plasma streamlines.
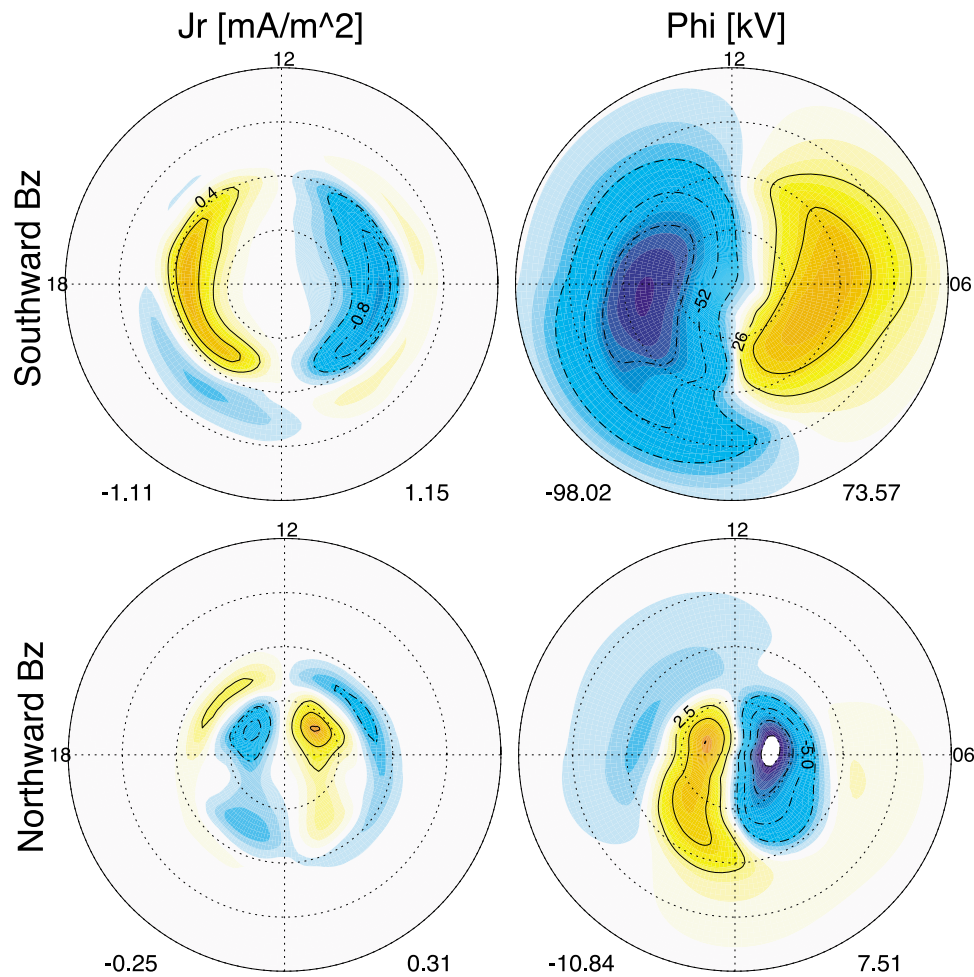
Figure 5. Ionospheric maps of (left) radial field-aligned current and (right) potential patterns for southward and northward IMF B_Z conditions. Yellow contours are positive values; blue are negative. Maximum and minimum values for each plot are shown to the lower right and left of the circle.

plasma sheet. The plasma is heated as it passes near the magnetic x-line, and then it is heated further as it moves earthward adiabatically. At the temperature peak (approximately 17.5 keV), the plasma begins to electromagnetically drift perpendicular to the plane of the plot. Though the streamline appears to stop, the component of the velocity perpendicular to the plane of Figure 3 has grown much larger than the earthward component, so the streamline can no longer be followed in this plane. Through this motion, ionospheric plasma is brought into the plasma sheet and is heated to contribute to the ring current.

3.2. Northward IMF

[17] The first idealized simulation was repeated, but at the 4 h mark, the IMF B_Z orientation was flipped from −10 nT to +10 nT. The magnetospheric configuration and plasma content after large-scale dynamics settled are shown in Figure 2 (right). The topology is what is expected for the solar wind drivers; reconnection over the cusps adds magnetic flux to the dayside and the tail region is inflated. In stark contrast to the southward IMF case, solar wind plasma has entered several regions in the magnetosphere where it was not found before. Most importantly, solar wind protons dominate the plasma sheet density.

[18] Figure 4 compares and contrasts the two cases to help explain the differences in plasma sources. Contours again show plasma content, but the dark lines now show flow streamlines. Figure 4 (left) presents the southward IMF case, while Figure 4 (right) presents the northward case. Plots in the top row are cuts of the magnetosphere in the Y = 0 plane (same as Figure 2) and there are tremendous differences between flow patterns in this plane for the different solar wind drivers. Figure 4 (upper left) expands upon the plasma flow illustrated in Figure 3.

[19] These flow patterns are what is expected when magnetospheric convection of field lines, as described by *Dungey* [1961], is superposed with plasma motion parallel to the field lines. The Dungey paradigm for convection is the flow of field lines away from the dayside reconnection point to the nightside reconnection zone, then from the nightside reconnection region back earthward, and eventually returning to the dayside. The path takes the field lines directly over (under) the north (south) pole, then equatorward as the field lines are brought together in the plasma sheet. This flow combined with the outflowing of the ionospheric plasma is equivalent to the flow description of Figure 3 and can occur only during southward IMF conditions.
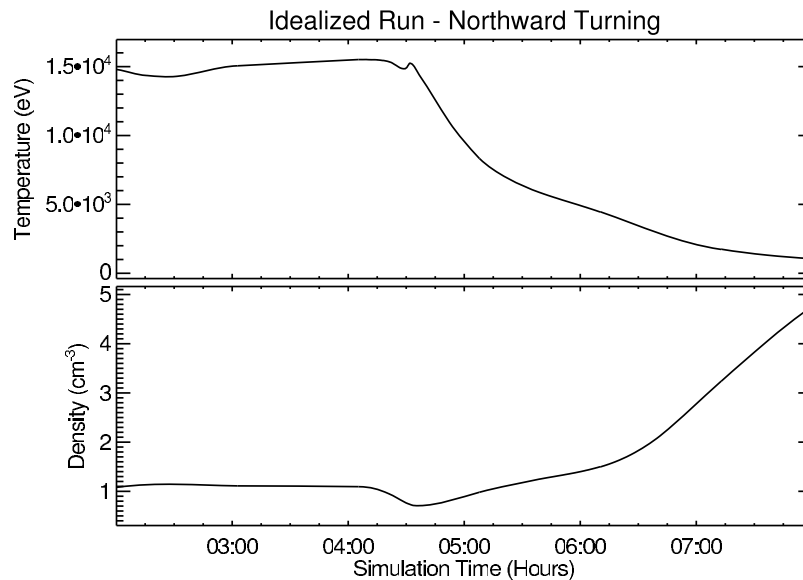
Figure 6. Time profile of temperature and density at $7R_E$ down tail. At 4 h into the simulation, IMF B_Z turns southward to northward.

[20] The flow pattern changes drastically for the northward IMF case (Figure 4, upper right). In the now predominately solar wind tail, flow lines diverge from a flow reversal region that is spatially larger and nearer to the Earth than what is seen in the southward IMF case. Patterns no longer reflect that of what would be expected in a "Dungey-type" magnetosphere.

[21] Plots in the bottom row are cuts in the equatorial plane (Z = 0) and further explain the dynamics seen in the top row. For the southward IMF case (Figure 4, bottom left), the plasma sheet and inner magnetosphere are flanked by large flow vortices. These vortices are driven by numeric diffusion of particles and momentum across the magnetopause and allow mixing of the two species defined in the model. Such features are indicative of viscous interaction between the magnetosphere and the solar wind populations, driving magnetosphere convection, a mechanism first proposed by *Axford and Hines* [1961]. Although these vortices are important, they are not the dominant convection method for the southward IMF case. Dungey-type convection brings in the majority of central plasma sheet and ring current material into the tail from the top and bottom, not the sides. When this mechanism is shut off, as in the case of the northward IMF simulation (Figure 4, lower right), *Axford and Hines* [1961] convection becomes the dominant driver in the magnetosphere. The vortices are now capable of bringing in the solar wind species, which dominates the plasma sheet and ring current regions. This source becomes so important in the simulation that the only ionosphere-source plasma found in the equatorial plane is a tightly defined, corotating plasmasphere.

[22] The differences arising from the different driving mechanisms are seen in the ionosphere as well. Ionospheric radial current and potential patterns for each IMF configuration are shown in Figure 5. The top row displays results from the southward IMF simulation; the bottom row displays results from the northward IMF case. Field-aligned currents are on the left and electric potentials on the right.

During the negative B_Z periods, the model produces the expected two-cell potential pattern and region 1 field-aligned currents [*Dungey*, 1961; *Iijima and Potemra*, 1976; *Lester et al.*, 2006]. For northward IMF, a four-celled potential pattern emerges where the poleward pair is reversed in polarity compared to the southward IMF case. This convection pattern is the well-known NBZ pattern (named for its association with northward IMF conditions) [*Burke et al.*, 1979; *Iijima et al.*, 1984; *Reiff and Heelis*, 1994; *Huang et al.*, 2000]. The lower-latitude field-aligned currents map to the viscous-driven flow vortices seen in Figure 4. The coupled numerical models' ability to clearly reproduce well-known features in the magnetosphere for both IMF orientations lends support to the results of the idealized runs.

[23] Changes in the plasma sheet due to IMF configuration are illustrated in Figure 6. Figure 6 (top) is a time series of plasma temperature at X = $-7R_E$ (X = Y = 0); Figure 6 (bottom) is the same but for number density. Before the northward turning, the ionosphere plasma is well heated because it enters near the magnetic x line and must travel the length of the tail, adiabatically heating for the duration of the trip. After the IMF northward turning, which occurs 4 h into the simulation, solar wind plasma enters through the flanks (as demonstrated in Figure 4). This plasma is significantly cooler because it experiences much less adiabatic heating by the time it reaches the point of measurement. This mechanism also brings in more plasma than its *Dungey* [1961] counterpart, creating a cold, dense plasma sheet, another well-studied feature of the magnetosphere [*Lennartsson and Shelley*, 1986; *Lennartsson*, 1992; *Terasawa et al.*, 1997; *Fujimoto et al.*, 1998; *Phan et al.*, 2000; *Huang et al.*, 2002] which has been established as consisting of solar wind plasma [*Lennartsson*, 1992; *Fujimoto et al.*, 1998].

3.3. Pressure Effects

[24] To test the effects of changing dynamic pressure on plasma sources, the southward IMF simulation was repeated, but the solar wind number density was increased from
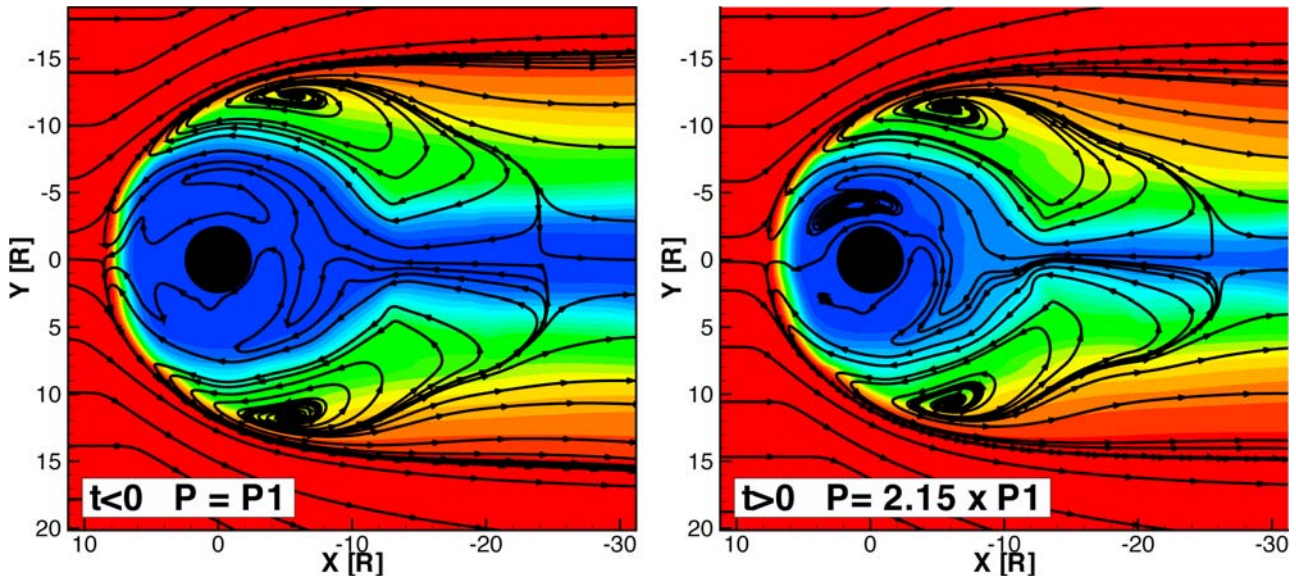
Figure 7. Equatorial cuts of the magnetosphere showing content and plasma streamlines, similar to Figure 4 (left) before the pressure increase ($t < 0$) and (right) afterward ($t > 0$). The pressure increases by a factor of 2.15.

8.7 cm^{-3} to 18.7 cm^{-3}, raising the dynamic pressure by a factor of 2.15. The increase occurred over the span of 1 min, similar to short timescale pressure increases observed in the solar wind that often signifies the onset of a magnetic storm. Again, the simulation was allowed to settle after the pressure increase.

[25] Figure 7 shows slices of the magnetosphere taken in the equatorial plane both before and after the pressure increase. As in Figure 4 (bottom), the contour shows the percent of the plasma that is of solar wind origins. Figure 7 (left) displays the now familiar configuration of the magnetosphere during southward IMF, where both reconnection and viscous interaction driven convection are acting on the magnetosphere. Figure 7 (right) shows the configuration after the pressure increase. The flank vortices have grown in size and have constricted the inner magnetosphere as well as the central plasma sheet, which is still drawing in ionospheric plasma through nightside reconnection. This is due to the solar wind dynamic pressure constricting the size of the magnetosphere as well as the increase in solar wind momentum, which strengthens the vortices. As the vortices are forced toward the center of the plasma sheet, solar wind plasma begins to diffuse into earthward flow, mixing with ionosphere plasma. This demonstrates that the two modes of
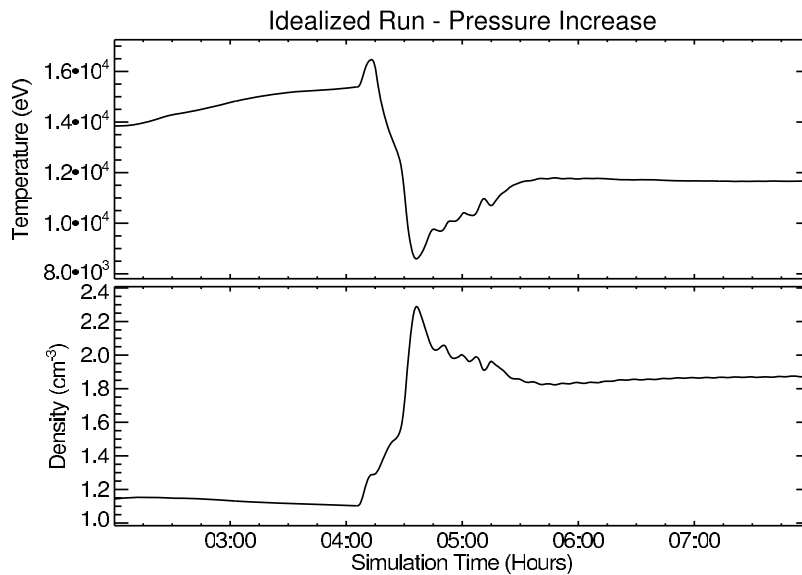

Figure 8. Same as Figure 6 but for the pressure increase simulation. The pressure increases sharply at 4 h into the simulation.
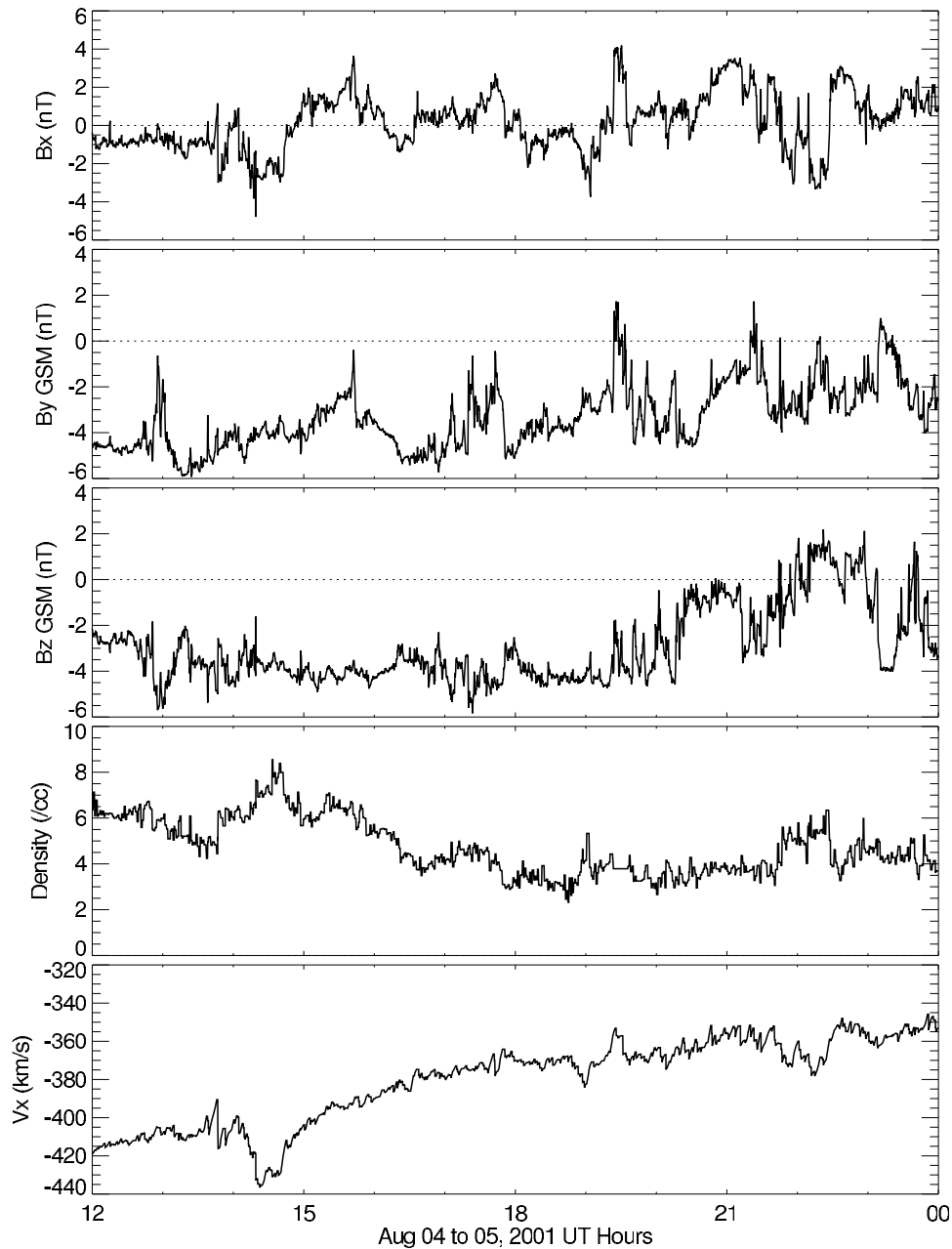
Figure 9. Solar wind drivers for the 4 August 2001 event study. Shown from top to bottom are the three components of the IMF, proton number density, and flow velocity in the X direction, where negative values indicate earthward flow. All values were observed by the ACE spacecraft and time shifted from the L1 point to the upstream boundary of the simulation's spatial domain.

driving are in a constant balance that depends on dynamic pressure and $-B_Z$ driven reconnection.

[26] Figure 8 demonstrates the effect on the central plasma sheet temperature and density $7R_E$ down tail. Similar to the effects on the plasma sheet due to a northward turning of the IMF, flank delivery of solar wind plasma increases the density and decreases the temperature. This feature is not nearly as strong as what is seen in Figure 6 because the IMF remains southward and thoroughly heated ionospheric plasma is still dominant. The results here provide an explanation for the observations of *Thomsen et al.* [2003], who found that cold, dense plasma sheet material could

penetrate the inner magnetosphere by means of a solar wind pressure pulse.

4. Event Analysis

4.1. Event of 4 August 2001

[27] The first real world event studied is 4 August 2001, spanning from 1200 UT to the end of the day. The solar wind conditions as measured by the ACE spacecraft used to drive the simulation are shown in Figure 9. This event features a nearly constant -4 nT IMF B_Z (Figure 9, center) for the first 9 h, at which point it slowly rotates northward.
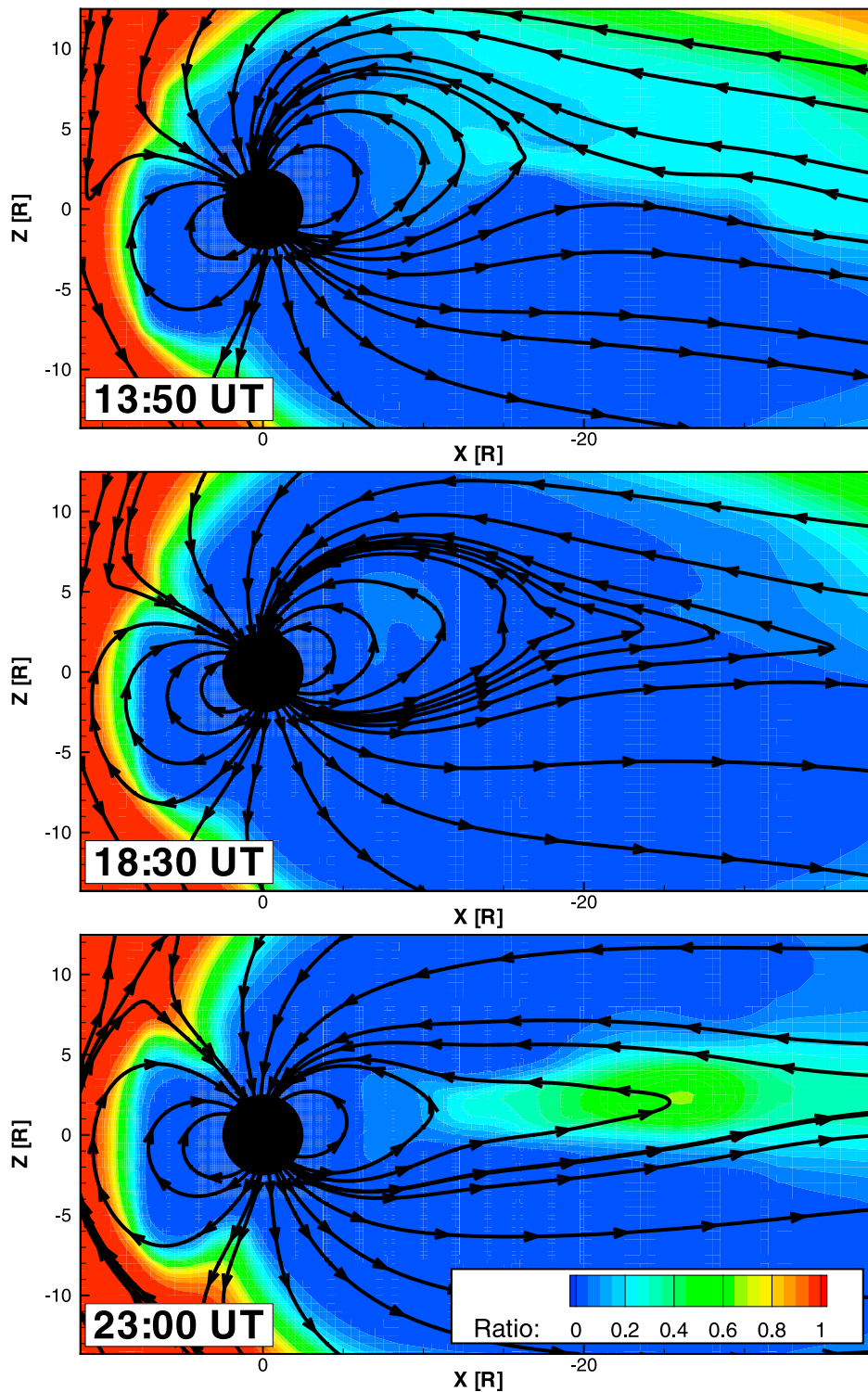
Figure 10. Y = 0 slices of the magnetosphere showing content and field lines (similar to Figure 2) from three separate epochs during the 4 August 2001 event.

The number density and velocity (Figure 9, bottom) both decrease smoothly and slightly during the first 4 h, reducing the dynamic pressure of the solar wind during this period. The solar wind is reasonably steady and this would not be considered strong magnetospheric driving conditions.

[28] The results of the simulation are summarized in Figure 10, which shows three plots of the magnetosphere similar to those shown in Figure 2. The results of this event agree with the entry mechanisms predicted by the idealized runs. Early in the simulation, solar wind conditions favor viscous driving and some solar wind plasma gets into the
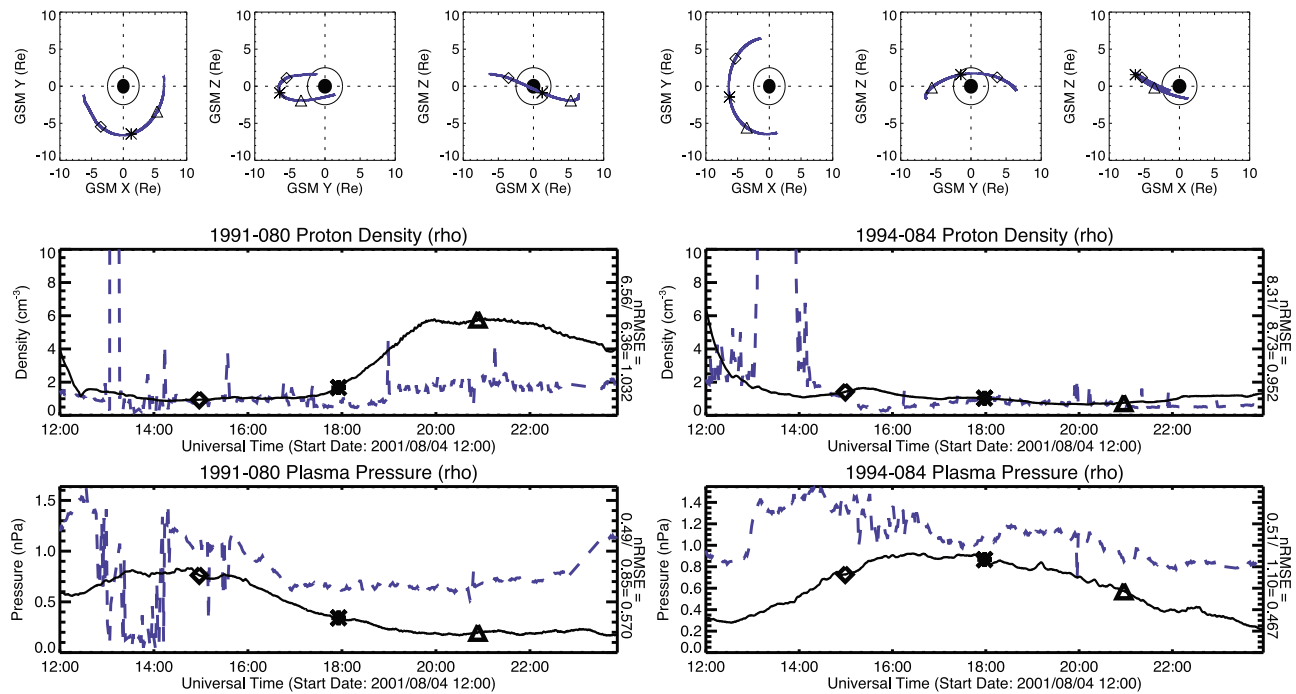
Figure 11. Data-model comparisons for the 4 August 2001 event, showing the comparisons for (left) the Los Alamos National Laboratory (LANL) 1991-080 geosynchronous satellite and (right) the 1994-084 satellite. Also shown is (top) the position of the satellite in the Z, X, and Y = 0 planes (markers in the position plots correspond to the markers in the plots below), (middle) number density, and (bottom) plasma pressure comparisons. Blue dashed lines are in situ measured data; black lines are results from the simulations.

plasma sheet through the flanks (Figure 10, top, taken at 1350 UT). This effect is diminished as the solar wind dynamic pressure is reduced (Figure 10, center, 1830 UT). After this time, as the B_Z component of the IMF turns northward, flank entry of solar wind plasma is detected (Figure 10, bottom, 2300 UT). Overall, the additional complexities of real world drivers and terrestrial field tilt provided minimal changes to the conclusions of the idealized simulations.

[29] During this time period, there are two Los Alamos National Laboratory (LANL) geosynchronous satellites that pass through the nightside of the magnetosphere. This location is where the ring current and plasma sheet region overlap, making it a key area to investigate the source of ring current and inner magnetospheric plasma. The results of the simulation are compared against data coming from the Magnetospheric Plasma Analyzer (MPA) instrument aboard these satellites. The MPA instruments are electrostatic analyzers that measure the energy-per-charge distribution. Temperature and density moments are calculated from this data for two energy windows: "cold" (0–100 eV for protons, 0–30 eV for electrons) and "hot" (100 eV or 30 eV up to 45 keV). The cold and hot moment densities are added together to produce a total plasma mass density and pressure. These values are easily comparable to results from the BATS-R-US model.

[30] Figure 11 shows the data-model comparisons along the two LANL spacecraft trajectories. Figure 11 (left) is the comparison for the 1991-080 spacecraft; Figure 11 (right) is for the 1994-084 satellite. The satellite's position is shown in the top row, with proton number density and pressure given in the next two rows. The blue dashed lines are in situ measurements; black lines are simulated values. While the satellites are on the nightside of the magnetosphere, density values show excellent agreement. MHD pressure is consistently too low but comes close to the measured pressure when the satellites are nearest to local midnight. The only exception to both of these results is during a brief moment of very cold, dense plasma, simultaneously observed by both satellites near 1300 UT. As the 1991-080 satellite reaches the dayside, both measured and simulated number densities increase, but the MHD density becomes almost twice as much as the measured. The too large densities on the dayside, as well as the low pressure on the nightside, are persistent features of MHD results. The latter likely is a result of insufficient adiabatic heating due to the understretched (hence shorter) tail in BATS-R-US, a feature noted by *Glocer et al.* [2009a] for MHD simulations not coupled to a driven model of polar wind outflow. The former feature will be discussed later.

[31] The excellent agreement with both satellite measurements while in the plasma sheet region demonstrates that the amount of plasma present is predicted very well by the BATS-R-US model. While this data set does not give an indication of whether the plasma is of ionospheric or solar wind origin, the fact that the MHD code appears to model the density correctly gives credence to the mechanisms observed in the simulations. It demonstrates that the results from the idealized and real world simulations are reasonable representations of the magnetosphere.
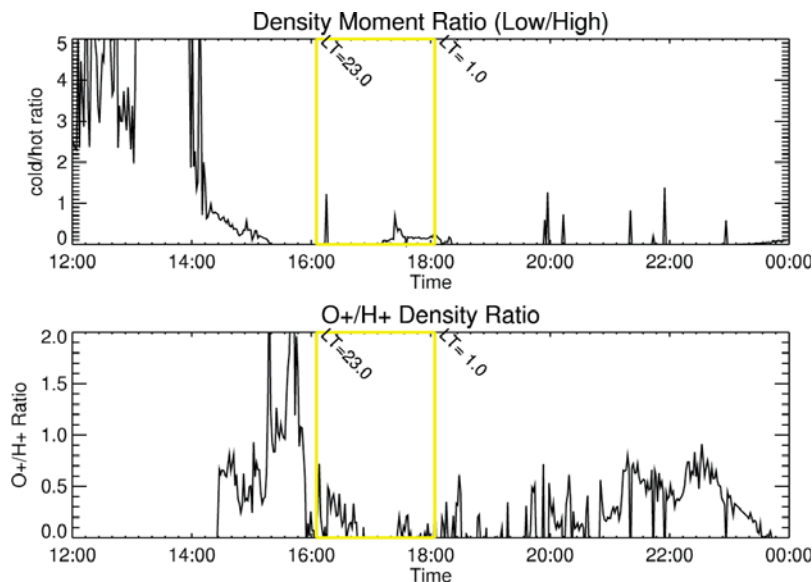
Figure 12. Plasma content information from the 1994-084 satellite, showing (top) the ratio of cold (0–100 eV) to hot (0.1–45 keV) plasma density and (bottom) the ratio of inferred oxygen to hydrogen number density. The inferred oxygen content is only considered valid when the cold to hot density ratio is very low and when the satellite is within a few hours of local midnight, a region denoted by the yellow boxes.

[32] To determine the source of the plasma, ion composition of the plasma sheet is required. For example, the presence of oxygen is a good indicator that the plasma is of ionospheric origins. The MPA instrument does not differentiate ion type, but oxygen content can be inferred from the moment data. The process, detailed by *Denton et al.* [2005], begins with the simple statement of charge neutrality given by

$$N_{HE} = N_{H^+} + N_{O^+} \qquad (2)$$

where N_{HE} is the hot electron density moment. Equation (2) neglects other ions and assumes that the hot electron and ion populations are much denser than the cold populations. From the calculation of the velocity distribution function [*Thomsen et al.*, 1999], the contribution to the total number density by ions of mass m_i is $\sqrt{m_p/m_i}$ (1/4 for singly ionized oxygen). Hence the hot proton density moment, N_{HP}, is given by

$$N_{HP} = N_{H^+} + N_{O^+}/4 \qquad (3)$$

Combining equations (2) and (3) yields

$$\frac{N_{O^+}}{N_p} = \frac{4(N_{HE} - N_{HP})}{(4N_{HP} - N_{HE})} \qquad (4)$$

When the MPA instrument indicates the presence of O^+, the plasma has an ionospheric component, while when there is no O^+ content, there is likely little ionospheric content.

[33] For this calculation to be valid, the ratio of cold to hot density moments (N_{LP}/N_{HP}, where N_{LP} is the low-temperature proton density moment) must be negligible. Additionally, away from local midnight, electrons are shielded from the inner magnetosphere [*Korth et al.*, 1999]

and the quasi-neutrality assumption breaks down. Hence this ratio is only valid within a few hours of local midnight. Despite these restrictions, this method for inferring O^+ in the plasma sheet allows further verification or rejection of the BATS-R-US results.

[34] The only useful data set for this analysis during the August 2001 event is from the 1994-084 satellite. The results are shown in Figure 12; Figure 12 (top) shows the N_{LP}/N_{HP} ratio and Figure 12 (bottom) shows the N_{O^+}/N_{H^+} ratio. The inference is valid in the region denoted by the yellow window, which is centered over local midnight and stretches 1 h local time in each direction, and when the N_{LP}/N_{HP} ratio is much less than 1. During these times, the N_{O^+}/N_{H^+} reaches ~30%, demonstrating ionospheric origins of the plasma sheet material. As described above, during this time period, the MHD code indicated that the plasma sheet was dominated by ionospheric plasma. This analysis indicates that the results of the simulation reasonably reflect the real world processes.

4.2. Event of 2 September 2004

[35] Figure 13 shows the IMF and solar wind conditions for 2 September 2004, which features a persistent, yet weak, northward IMF B_z (Figure 13, top) as well as nearly constant number density and velocity (Figure 13, bottom). There are several southward turnings, most notably at 1415 UT. This event was chosen to investigate the veracity of the northward IMF idealized results.

[36] The results of this simulation are consistent with the idealized results, but the southward turnings throughout the event demonstrate the interplay between the two prevalent driving mechanisms. Figure 14 (left) shows the configuration and content of the magnetosphere at 1410 UT, during northward IMF but immediately before the southward turning. Solar wind plasma is present in the plasma sheet but
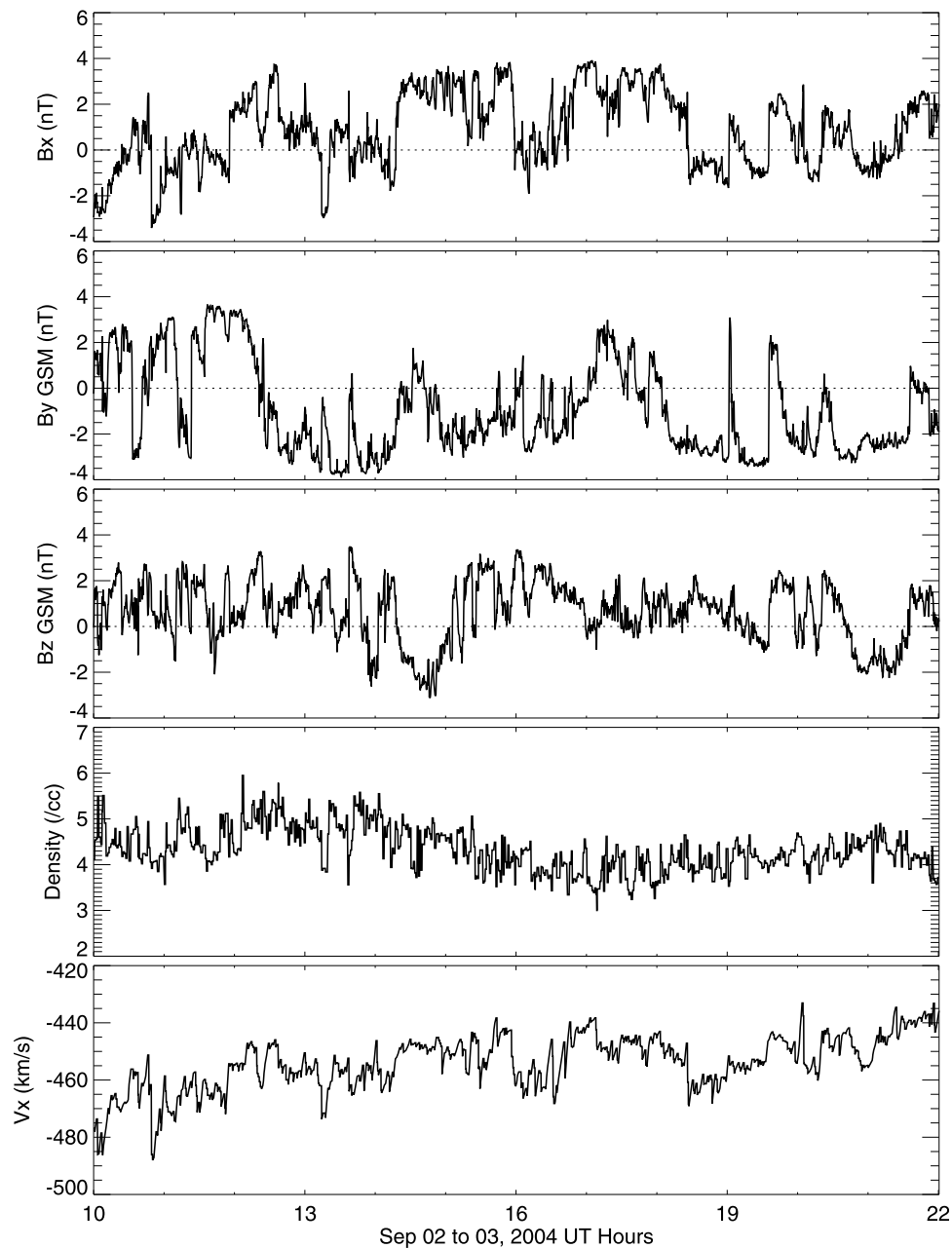
Figure 13. Same as Figure 9 but for the 2 September 2004 event.

quickly drains after the turning. An hour later (Figure 14, right), ionosphere plasma dominates the plasma sheet, only to be quickly replaced as the IMF turns northward again. The two sources are constantly changing the content as the event continues.

[37] This interplay is reflected in data from the LANL-97A satellite, which passes through local midnight during this event. Figure 15 shows the data-model comparison for this satellite. At 1430 UT, the number density drops (Figure 15, center, blue line) while the plasma pressure increases (Figure 15, bottom, blue line). This behavior is what is expected if what is predicted by the model is correct; for northward IMF, the colder, denser plasma sheet forms through solar wind flank entry, but during even weak

southward turnings, ionosphere plasma enters via tail reconnection and is warmed adiabatically to temperatures greater than the flank-entering solar wind plasma.

[38] The model results, seen in Figure 15 as the black, solid lines, capture the pressure jump but not the density drop. Examining the position of this satellite with relation to the plasma sheet in Figure 14, the satellite is just within the boundary of the solar wind dominated plasma sheet, so it does not observe the denser flank plasma during the simulation. Noting that the solar wind dynamic pressure is weaker than what is used in the idealized northward IMF simulation, where flank-entering, solar wind plasma reached deeper into the magnetosphere, it is likely that BATS-R-US is underpredicting the strength of the viscous driving.
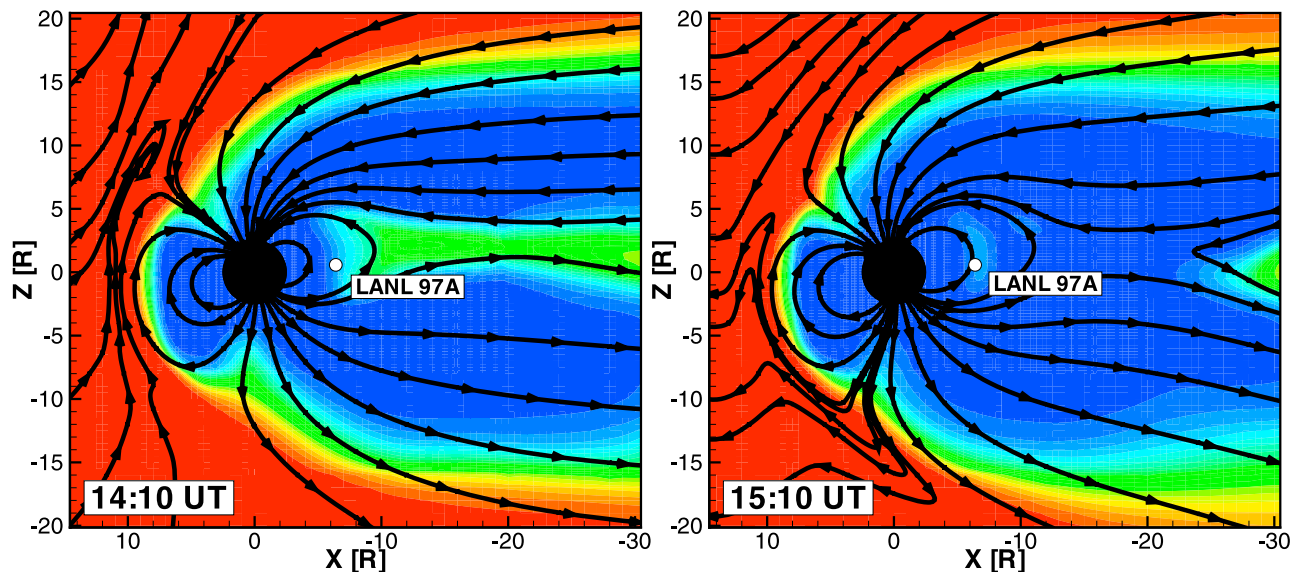
Figure 14. Similar to Figure 10 but for the 2 September 2004 event. The position of the LANL-97A satellite is shown as the labeled white dot in each frame.

[39] Analysis of possible oxygen content for this satellite is shown in Figure 16. The ratio of cold to hot plasma density remains high for most of the event, as expected given the northward IMF conditions. Around 1430 UT, however, this ratio dives to values significantly less than 1, yielding a narrow time period within the yellow box where a proper inference about the O^+ content of the plasma sheet can be made. During this brief time, N_{O+}/N_{H+} reaches ~20%, revealing that the population is likely of ionospheric source. These results further support the idealized simulation results.

5. Discussion

[40] The results of this study suggest that the magnetosphere has two modes of driven dynamics, each providing its own source and entry mechanism of plasma into the central plasma sheet and inner magnetosphere. The modes are dependent on solar wind conditions. They are not mutually exclusive; there is a constant interplay between each other depending on the ram pressure and IMF orientation and strength.

[41] The results presented here are supported by previous numerical studies. The ionospheric dominance of the plasma sheet during southward IMF conditions was predicted by *Chappell et al.* [1987, 2000]. Good agreement is found with the true multifluid simulations of *Winglee* [1998] and *Winglee* [2000] for southward IMF cases and solar wind dominance during northward IMF. *Huddleston et al.* [2005] predicts entry paths for ionospheric plasma into the central plasma sheet via particle tracing routines that qualitatively mirror those shown in Figure 3. *Peroomian and El-Alaoui* [2008] finds flank entry to be an appreciable, but not dominant, entry path for solar wind particles during storm time conditions.

[42] Comparisons to data investigations are both favorable and questionable. The ionosphere as a strong contributor of magnetospheric plasma is supported by a plethora of works

[*Lennartsson and Shelley*, 1986; *Nosé et al.*, 2003; *Denton et al.*, 2005]. As was mentioned earlier, the results for northward IMF provide unifying explanations for observations of the cold, dense plasma sheet [*Lennartsson and Shelley*, 1986; *Lennartsson*, 1992; *Terasawa et al.*, 1997; *Fujimoto et al.*, 1998; *Phan et al.*, 2000; *Huang et al.*, 2002] as well as the NBZ potential pattern [*Burke et al.*, 1979; *Iijima et al.*, 1984; *Reiff and Heelis*, 1994; *Huang et al.*, 2000]. The balance between the two entry mechanisms governed by solar wind conditions, as in Figures 7 and 8, provides a potential explanation for unexpected cold ions observed in the hot plasma sheet [e.g., *Seki et al.*, 2003]. More recent work by *Nagata et al.* [2008], which uses a large data set to determine the correlation between magnetospheric number density and solar wind conditions in 3-D space, has some striking similarities to the conclusions drawn here. They find a strong dependence on IMF Bz for plasma number density closer to Earth and in the central plasma sheet, suggesting ionospheric contributions to these regions. Other regions correlate better with solar wind plasma number density, suggesting solar wind source. The apparent solar wind and IMF control of magnetospheric number density is similar to what is found here. However, by closely examining the 3-D distributions of the correlations, *Nagata et al.* [2008] attribute solar wind plasma entry to reconnection-type processes. Potential reasons for this important discrepancy are discussed below.

[43] There are important differences found in other investigations, most notably solar wind access to the plasma sheet via dayside reconnection. Both *Peroomian and El-Alaoui* [2008] and *Winglee* [2003] observe solar wind particles in the plasma sheet that entered from the dayside reconnection site in particle tracing results during storm time periods. *Moore et al.* [2005] finds this to be the dominant source for plasma sheet mass during constant southward IMF conditions when both solar wind and ionospheric source populations are traced through MHD-generated
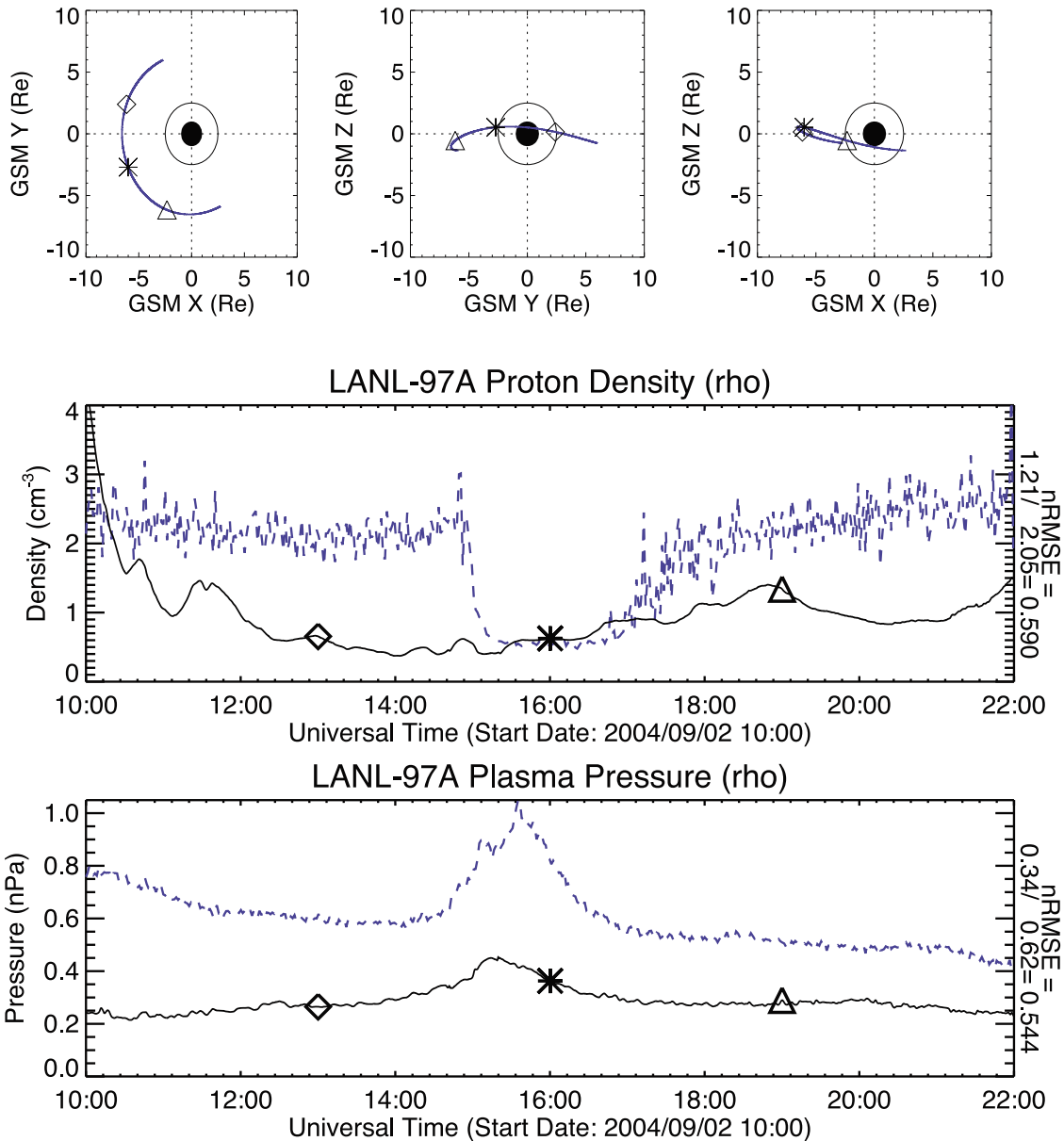
Figure 15. Same as Figure 11 but for the LANL-97A satellite during the 2 September 2004 event.

fields. In the results presented here, this entry mechanism is unavailable to the solar wind species.

[44] This difference illustrates a key limitation in the methodology applied here. Because the individual species evolve as a single fluid (they share momentum and energy equations), the outflowing ionosphere plasma acts to shield solar wind plasma from moving earthward and deep into the cusps along open magnetic field lines through pressure balance. Although there is observational and numerical evidence for solar wind particles deep in the cusp regions [e.g., *Escoubet et al.*, 2008], the single fluid "pressure shielding" effects prevent it here. Mixing of the two species along field lines is controlled by numerical diffusion in the solution of the continuity equations, which is too weak to allow penetration of the solar wind species to regions earthward of the magnetic x line in the central plasma sheet.

This may mean that these results are contingent on the inner boundary number density and that a true multifluid simulation would allow an appreciable entry of solar wind plasma through reconnection driven convection.

[45] Figure 17 addresses the first of these concerns. Figure 17 (top) again shows the results for the 4 August 2001 event at the 1991-080 satellite, shown earlier as Figure 11 (center). During this simulation, the inner boundary number density was held constant over the entire boundary at a value of 28 cm^{-3}, which was chosen to balance code stability with realistic conditions. Outflow in the coupled ionosphere-magnetosphere models occurs by diffusion of mass out of the inner boundary, which is then accelerated by the convection electric field (across field lines) as well as pressure gradients (primarily along field lines). To investigate the effects of reducing the inner
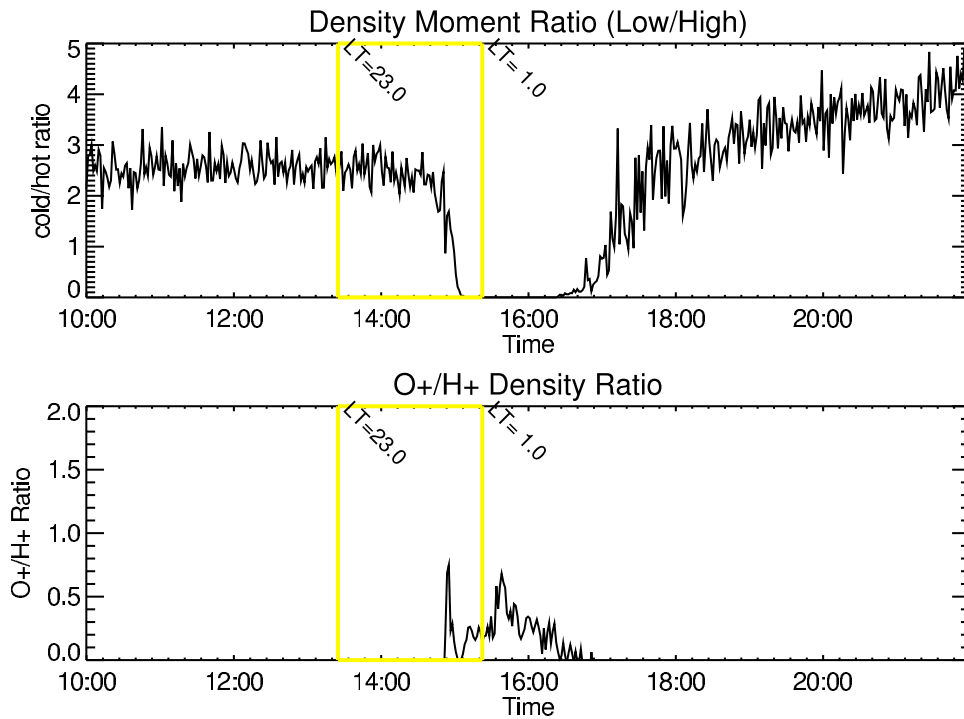
Density Moment Ratio (Low/High)

O+/H+ Density Ratio

Figure 16. Same as Figure 12 but for the LANL-97A satellite during the 2 September 2004 event.

1991-080 Density - Standard Inner Boundary Density

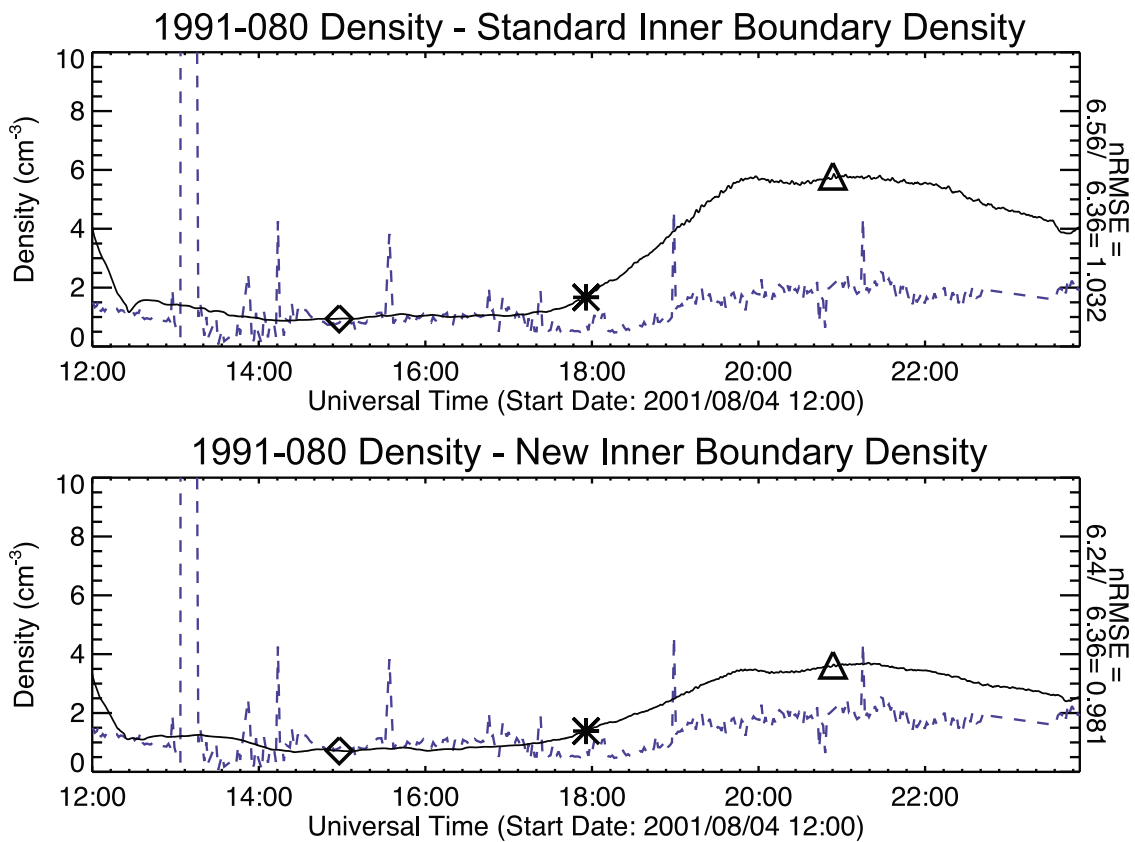## 1991-080 Density - New Inner Boundary Density

Figure 17. Comparisons of number density at geosynchronous orbit for standard BATS-R-US inner boundary density (28 cm^{-3}) (same as Figure 11) and new, realistic inner boundary density (17 cm^{-3}).

boundary density, the value was lowered to 17 cm^{-3} and the simulation performed again. This number is consistent with what is used in the work of *Huddleston et al.* [2005] and was generated from surface charging corrected TIDE measurements originally presented by *Su et al.* [1998]. Figure 17 (bottom) demonstrates that in the night hemisphere, there is very little difference between the results when the inner boundary density is changed. The density on the dayside is reduced, improving agreement between the data and the model. The species content did not change. Hence density inner boundary conditions are unimportant to central plasma sheet composition when this simplified outflow is used but do control the dayside plasma density.

[46] On the dayside of the magnetosphere, the field lines are convecting slowly around the magnetosphere and have ample time to fill with ionospheric plasma until pressure balance is achieved between plasma in a flux tube and the ionospheric plasma pressure at the flux tube foot point. By lowering the inner boundary density, the foot point pressure is lowered, and equilibrium is achieved at lower densities at equatorial locations. The data-model comparisons at the day side of the magnetosphere in Figure 11 demonstrate that at least for this time period, the density inner boundary condition used are too high. Because ionospheric outflow is dynamic and dependent on solar activity [*Yau and André*, 1997], dynamic inner boundary conditions could improve results [*Glocer et al.*, 2009a, 2009b].

[47] As for the second concern, a true multifluid simulation allows for counterstreaming populations, which could potentially allow significant solar wind entry into the central plasma sheet. While some solar wind entry is expected when such a system is used, the initial evidence is that this contribution would be much less than the ionospheric contribution, as demonstrated by *Glocer et al.* [2009a]. The consistently under stretched field lines for simple outflow simulations, especially during storm times, imply that the basic outflow generated in the MHD code is underpredicting the actual mass outflow. When the realistic, heavy ion outflow was modeled in the work of *Glocer et al.* [2009a] and used as inner boundary conditions to BATS-R-US MHD, it increased inner magnetosphere pressure, vastly improving the magnetic field results at geosynchronous orbit. It was the increase in the ionospheric source, not the solar wind source, that produced more realistic model results. This work was repeated using multifluid MHD [*Glocer et al.*, 2009b] with similar results: the additional mass outflow improved MHD results. *Glocer et al.* [2009b] compared the modeling results to Cluster density and composition measurements and found good agreement. Effects of increasing outflow can be seen by the similar studies of *Moore et al.* [2005] and *Huddleston et al.* [2005]; both used similar methodologies, but the latter used an increased outflow flux and velocity by reexamining TIDE data and adjusting for spacecraft charging. While *Moore et al.* [2005] found that ionospheric sources were secondary compared to solar wind sources, *Huddleston et al.* [2005] found that the ionosphere, using the increased outflow, could easily account for all plasma sheet mass. While these works support the conclusion that the ionosphere is the dominant source of plasma for southward IMF, they do not reject the notion that reconnection entry of solar wind plasma could be an appreciable source. To fully explore the solar wind contribution during southward IMF conditions, true multispecies MHD must be used.

[48] Another important difference between these results and others is the predominance of flank entry for northward IMF as opposed to high-latitude entry at cusp reconnection points, found in the results of *Moore et al.* [2005] and *Winglee* [2000]. As seen in the northward IMF results of Figures 2 and 4, NB_Z-type reconnection is occurring and drawing in solar wind plasma into the dayside magnetosphere. However, the flow of this plasma is overcome by the flank vortices, and rather than moving toward the nightside, it is swept around the flanks. This may indicate an overprediction of the strength of the viscous driving. It may be argued that the formation of the solar wind dominated boundary layer seen in this study is the result of NB_z reconnection and transport as described by *Song and Russell* [1992]. Because the layer is present for both northward and southward orientations, it is not likely that the *Song and Russell* [1992] mechanism is dominant.

[49] The role of numerical diffusion in this study is also a concern, despite the steps taken to reduce it. An investigation was performed to ensure that the results are not numerical artifacts. The 8 h southward IMF idealized simulation was repeated using the same settings, but with a far lower resolution (minimum $\frac{1}{4}R_E$ grid size, approximately 200,000 cells). This was again repeated using the settings and grid layout described in section 2 but with a Boris correction factor of 0.005 (reduced by a factor of 4) to greatly reduce the diffusion. Between these two configurations and the one employed for this study, no outstanding qualitative differences were found. In other words, the entry mechanisms described here could not be changed by altering the code setup. While this finding is encouraging, a thorough, quantitative study of the role of numerical diffusion is required.

[50] Finally, the LANL geosynchronous data used in this study provides confidence to the conclusions drawn in this work, but ion composition is a data product and not a direct measurement. To truly confirm the conclusions, mass resolving instruments must be used to get measured, not inferred, ion composition. Though the geosynchronous measurements were selected for their excellent spatial and temporal coverage, future work must include mass resolving instruments along with several additional event studies.

6. Conclusions

[51] This study used the multispecies version of BATS-R-US to investigate the source population and entry mechanism of plasma sheet and inner magnetosphere material. Using simulation results, we assert that (1) during southward IMF, the central plasma sheet and inner magnetosphere are dominated by plasma of ionospheric origin; (2) during northward IMF, the central plasma sheet is dominated by plasma of solar wind origin; and (3) the solar wind dynamic pressure helps to regulate the amount of solar wind plasma in the plasma sheet, with higher pressure leading to more solar wind entry. These assertions are verified for two nonstorm time periods through comparisons between model results and LANL MPA data.

[52] Future work will address several issues, most notably the size, shape, and dynamics of the viscous interaction cells residing in the flanks. As these regions control the balance between the delivery of the two plasma populations into the plasma sheet, understanding them as well as the responsible numerical diffusion is key. Additionally, important time-scales must be investigated, such as the travel time of the plasma from the ionosphere to the inner magnetosphere and time to switch from one driving mode to the other. These items require many more simulations as well as further data comparisons to validate the results.

References

Axford, W. I., and C. O. Hines (1961), A unifying theory of high-latitude geophysical phenomena and geomagnetic storms, *Can. J. Phys. Rev.*, *39* (10), 1433–1464.

Boris, J. P. (1970), A physically motivated solution of the Alfvén problem, *Memo. Rep. 2167*, Nav. Res. Lab., Washington, D.C.

Burke, W. J., M. C. Kelley, R. C. Sagalyn, M. Smiddy, and S. T. Lai (1979), Polar cap electric field structures with a northward interplanetary magnetic field, *Geophys. Res. Lett.*, *6*, 21–24.

Chappell, C. R., T. E. Moore, and J. H. Waite Jr. (1987), The ionosphere as a fully adequate source of plasma for the Earth's magnetosphere, *J. Geophys. Res.*, *92*, 5896–5910.

Chappell, C. R., B. L. Giles, T. E. Moore, D. C. Delcourt, P. D. Craven, and M. O. Chandler (2000), The adequacy of the ionospheric source in supplying magnetospheric plasma, *J. Atmos. Sol. Terr. Phys.*, *62*, 421–436.

Denton, M. H., M. F. Thomsen, H. Korth, S. Lynch, J. C. Zhang, and M. W. Liemohn (2005), Bulk plasma properties at geosynchronous orbit, *J. Geophys. Res.*, *110*, A07223, doi:10.1029/2004JA010861.

De Zeeuw, D. L., T. I. Gombosi, C. P. T. Groth, K. G. Powell, and Q. F. Stout (2000), An adaptive MHD method for global space weather simulations, *IEEE Trans. Plasma Sci.*, *28*, 1956–1965.

Dungey, J. W. (1961), Interplanetary magnetic field and the auroral zones, *Phys. Rev. Lett.*, *6*, 47–48.

Eastman, T. E., L. A. Frank, and C. Y. Huang (1985), The boundary layers as the primary transport regions of the Earth's magnetotail, *J. Geophys. Res.*, *90*, 9541–9560.

Escoubet, C. P., et al. (2008), Two sources of magnetosheath ions observed by cluster in the mid-altitude polar cusp, *Adv. Space Res.*, *41*, 1528–1536, doi:10.1016/j.asr.2007.04.031.

Fujimoto, M., T. Terasawa, T. Mukai, Y. Saito, T. Yamamoto, and S. Kokubun (1998), Plasma entry from the flanks of the near-Earth magnetotail: Geotail observations, *J. Geophys. Res.*, *103*, 4391–4408.

Glocer, A., G. Tóth, T. Gombosi, and D. Welling (2009a), Modeling ionospheric outflows and their impact on the magnetosphere, Initial results, *J. Geophys. Res.*, *114*, A05216, doi:10.1029/2009JA014053.

Glocer, A., G. Tóth, T. Ma, Y. Gombosi, J. Zhang, and L. Kistler (2009b), Multifluid Block-Adaptive-Tree Solar wind Roe-type Upwind Scheme: Magnetospheric composition and dynamics during geomagnetic storms-Initial results, *J. Geophys. Res.*, *114*, A12203, doi:10.1029/2009JA014418.

Gombosi, T. I., G. Tóth, D. L. De Zeeuw, K. C. Hansen, K. Kabin, and K. G. Powell (2002), Semi-relativistic magnetohydrodynamics and physics-based convergence acceleration, *J. Comput. Phys.*, *177*, 176–205.

Huang, C.-S., G. J. Sofko, A. V. Koustov, D. A. Andre, J. M. Ruohoniemi, R. A. Greenwald, and M. R. Hairston (2000), Evolution of ionospheric multicell convection during northward interplanetary magnetic field with $|B_z/B_y|$ greater than 1, *J. Geophys. Res.*, *105*, 27,095–27,108, doi:10.1029/2000JA000163.

Huang, C.-S., J. C. Foster, P. Song, G. J. Sofko, L. A. Frank, and W. R. Paterson (2002), Geotail observations of magnetospheric midtail

during an extended period of strongly northward interplanetary magnetic field, *Geophys. Res. Lett.*, *29*(4), 1056, doi:10.1029/2001GL014170.

Huddleston, M. M., C. R. Chappell, D. C. Delcourt, T. E. Moore, B. L. Giles, and M. O. Chandler (2005), An examination of the process and magnitude of ionospheric plasma supply to the magnetosphere, *J. Geophys. Res.*, *110*, A12202, doi:10.1029/2004JA010401.

Iijima, T., and T. A. Potemra (1976), Field-aligned currents in the dayside cusp observed by Triad, *J. Geophys. Res.*, *81*, 5971–5979.

Iijima, T., L. J. Zanetti, and P. F. Bythrow (1984), Large-scale Birkeland currents in the dayside polar region during strongly northward IMF: A new Birkeland current system, *J. Geophys. Res.*, *89*, 7441–7552.

Korth, H., M. F. Thomsen, J. E. Borovsky, and D. J. McComas (1999), Plasma sheet access to geosynchronous orbit, *J. Geophys. Res.*, *104*, 25,047–25,062.

Lennartsson, O. W. (2001), Ion composition aspects of magnetotail plasma flows, *J. Geophys. Res.*, *106*, 15,621–15,634, doi:10.1029/2000JA000427.

Lennartsson, W. (1992), A scenario for solar wind penetration of Earth's magnetic tail based on ion composition data from the ISEE 1 spacecraft, *J. Geophys. Res.*, *97*, 19,221–19,238.

Lennartsson, W., and E. G. Shelley (1986), Survey of 0.1- to 16-keV/e plasma sheet ion composition, *J. Geophys. Res.*, *91*, 3061–3076.

Lester, M., G. Provan, and J. Wild (2006), Review of ionospheric effects of solar wind magnetosphere coupling in the context of the expanding contracting polar cap boundary model, *Space Sci. Rev.*, *124*, 117–130.

Lyon, J., J. Fedder, and C. Mobarry (2004), The Lyon-Fedder-Mobarry (LFM) global MHD magnetospheric simulation code, *J. Atmos. Sol. Terr. Phys.*, *66*, 1333–1350.

Ma, Y., A. F. Nagy, K. C. Hansen, D. L. De Zeeuw, T. I. Gombosi, and K. Powell (2002), Three-dimensional multispecies MHD studies of the solar wind interaction with Mars in the presence of crustal fields, *J. Geophys. Res.*, *107*(A10), 1282, doi:10.1029/2002JA009293.

Moore, T. E., et al. (2005), Plasma sheet and (nonstorm) ring current formation from solar and polar wind sources, *J. Geophys. Res.*, *110*, A02210, doi:10.1029/2004JA010563.

Nagata, D., S. Machida, S. Ohtani, Y. Saito, and T. Mukai (2008), Solar wind control of plasma number density in the near-Earth plasma sheet: Three-dimensional structure, *Ann. Geophys.*, *26*(12), 4031–4049.

Nosé, M., R. W. McEntire, and S. P. Christon (2003), Change of the plasma sheet ion composition during magnetic storm development observed by the Geotail spacecraft, *J. Geophys. Res.*, *108*(A5), 1201, doi:10.1029/2002JA009660.

Peroomian, V., and M. El-Alaoui (2008), The storm-time access of solar wind ions to the nightside ring current and plasma sheet, *J. Geophys. Res.*, *113*, A06215, doi:10.1029/2007JA012872.

Phan, T. D., R. P. Lin, S. A. Fuselier, and M. Fujimoto (2000), Wind observations of mixed magnetosheath-plasma sheet ions deep inside the magnetosphere, *J. Geophys. Res.*, *105*, 5497–5506.

Powell, K., P. Roe, T. Linde, T. Gombosi, and D. L. De Zeeuw (1999), A solution-adaptive upwind scheme for ideal magnetohydrodynamics, *J. Comput. Phys.*, *154*, 284–309.

Reiff, P. H., and R. A. Heelis (1994), Four cells or two? Are four convection cells really necessary?, *J. Geophys. Res.*, *99*, 3955–3959.

Ridley, A. J., and M. W. Liemohn (2002), A model-derived storm time asymmetric ring current driven electric field description, *J. Geophys. Res.*, *107*(A8), 1151, doi:10.1029/2001JA000051.

Ridley, A. J., K. C. Hansen, G. Tóth, D. L. De Zeeuw, T. I. Gombosi, and K. G. Powell (2002), University of Michigan MHD results of the GGCM metrics challenge, *J. Geophys. Res.*, *107*(A10), 1290, doi:10.1029/2001JA000253.

Ridley, A. J., T. Gombosi, and D. L. De Zeeuw (2004), Ionospheric control of the magnetospheric configuration: Conductance, *Ann. Geophys.*, *22*, 567–584.

Rusanov, V. (1961), Calculation of interaction of non-steady schock waves with obstacles, *J. Comput. Math. Phys.*, *1*, 267–279.

Seki, K., et al. (2003), Cold ions in the hot plasma sheet of Earth's magnetotail, *Nature*, *422*, 589–592.

Shelley, E. G., R. G. Johnson, and R. D. Sharp (1974), Morphology of energetic O+ in the magnetosphere, in *Magnetospheric Physics, Proceedings of the Advanced Summer Institute, Held at Sheffield, U.K., August, 1973, Astrophys. Space Sci. Libr.*, vol. 44, edited by B. M. McCormac, p. 135, D. Reidel, Dordrecht, Netherlands.

Song, P., and C. T. Russell (1992), A model of the formation of the low latitude boundary layer, *J. Geophys. Res.*, *97*, 1411–1420.

Su, Y.-J., J. L. Horwitz, T. E. Moore, B. L. Giles, M. O. Chandler, P. D. Craven, M. Hirahara, and C. J. Pollock (1998), Polar wind survey with the Thermal Ion Dynamics Experiment/Plasma Source Instrument suite aboard POLAR, *J. Geophys. Res.*, *103*, 29,305–29,338, doi:10.1029/98JA02662.

Terasawa, T., et al. (1997), Solar wind control of density and temperature in the near-Earth plasma sheet: WIND/GEOTAIL collaboration, *Geophys. Res. Lett.*, *24*, 935–938.

Thomsen, M., E. Noveroske, J. Borovsky, and D. McComas (1999), Calculation of moments from measurements by the Los Alamos magnetospheric plasma analyzer, *Tech. Rep. LA 135666-MS*, Los Alamos Natl. Lab., Los Alamos, N. M.

Thomsen, M. F., J. E. Borovsky, R. M. Skoug, and C. W. Smith (2003), Delivery of cold, dense plasma sheet material into the near-Earth region, *J. Geophys. Res.*, *108*(A4), 1151, doi:10.1029/2002JA009544.

Tóth, G., et al. (2005), Space weather modeling framework: A new tool for the space science community, *J. Geophys. Res.*, *110*, A12226, doi:10.1029/2005JA011126.

Tóth, G., D. L. D. Zeeuw, T. I. Gombosi, W. B. Manchester, A. J. Ridley, I. V. Sokolov, and I. I. Roussev (2007), Sun to thermosphere simulation of the October 28–30, 2003 storm with the Space Weather Modeling Framework, *Space Weather*, *5*, S06003, doi:10.1029/2006SW000272.

Winglee, R. M. (1998), Multi-fluid simulations of the magnetosphere: The identification of the geopause and its variation with IMF, *Geophys. Res. Lett.*, *25*, 4441–4444.

Winglee, R. M. (2000), Mapping of ionospheric outflows into the magnetosphere for varying IMF conditions, *J. Atmos. Terr. Phys.*, *62*, 527–540.

Winglee, R. M. (2003), Circulation of ionospheric and solar wind particle populations during extended southward interplanetary magnetic field, *J. Geophys. Res.*, *108*(A10), 1385, doi:10.1029/2002JA009819.

Yau, A., and M. André (1997), Sources of ion outflow in the high latitude ionosphere, *Space Sci. Rev.*, *80*, 1–25.

Zhang, J., et al. (2007), Understanding storm-time ring current development through data-model comparisons of a moderate storm, *J. Geophys. Res.*, *112*, A04208, doi:10.1029/2006JA011846.

A. J. Ridley, Department of Atmospheric, Oceanic and Space Sciences, 2455 Hayward St., University of Michigan, Ann Arbor, MI 48109-2143, USA.

D. T. Welling, Los Alamos National Laboratory, P.O. Box 1663, Los Alamos, NM 87545, USA. (dwelling@lanl.gov)